

Noise Scaling in SQUID Arrays

O. A. Nieves, K-H. Müller

CSIRO Manufacturing, PO Box 218, Lindfield, NSW 2070, Australia

E-mail: oscar.nieves@csiro.au

Abstract. We numerically investigate the noise scaling in high- T_c commensurate 1D and 2D SQUID arrays. We show that the voltage noise spectral density in 1D arrays violates the scaling rule of $\sim 1/N_p$ for the number N_p of Josephson junctions in parallel. In contrast, in 2D arrays with N_s 1D arrays in series, the voltage noise spectral density follows more closely the expected scaling behaviour of $\sim N_s/N_p$. Additionally, we reveal how the flux and magnetic field rms noise spectral densities deviate from their expected $\sim (N_s N_p)^{-1/2}$ scaling and discuss their implications for designing low noise magnetometers.

Keywords: noise, SQUID, array, scaling law

Submitted to: *Supercond. Sci. Technol.*

1. Introduction

Superconducting quantum interference devices, better known as SQUIDS; are used extensively in magnetic sensing applications [1, 2]. When multiple SQUIDS are combined in parallel and in series to form a so-called SQUID array, the response to externally applied magnetic fields can be enhanced and tuned via the number of Josephson junctions and the geometry of the SQUID cells [3–12]. Henceforth, SQUID and superconducting quantum interference filter (SQIF) arrays can be used as highly sensitive magnetometers and low-noise amplifiers in a variety of applications [13–18].

A commonly used characteristic of operation is the voltage-flux response. The SQUID array is current biased and any small applied magnetic flux $\delta\phi$ per loop is converted into voltage $\delta\bar{v}$ across the array. The conversion efficiency is given by the transfer function $\bar{v}_\phi = \partial\bar{v}/\partial\phi$. The electrical normal resistance of Josephson junctions (JJs) generates Johnson white noise, which causes the appearance of voltage and flux noise in SQUID arrays. Both the transfer function and the noise spectral densities depend on many device parameters. The problem of optimising the common dc SQUID has long been solved [19–21]. In contrast, optimising SQUID arrays is still a partially unsolved problem due to the larger parameter space and computational complexity. The transfer function of 1D and 2D arrays has been studied theoretically [22], but their noise spectral densities have not been simulated yet.

The current paper is organised as follows. In Sec. II we investigate the maximum transfer function of commensurate SQUID arrays with $N_p = 2$ –20 JJs in parallel and $N_s = 1$ –20 JJ rows in series for the case where temperature, critical current, normal resistance and partial inductances are kept constant. In Sec. III we explore the low-frequency voltage noise spectral density and the rms flux and magnetic field noise spectral densities, and their deviation from the expected scaling. Finally, we discuss some of the implications this has for the design of high- T_c SQUID arrays.

2. Array transfer function

We start by discussing the transfer function of 1D and 2D SQUID arrays, since the transfer function is

needed to calculate the flux noise and magnetic field noise spectral densities. We assume that the JJs of the SQUID arrays are over-damped, a valid assumption for YBCO thin film arrays at 77 K, and all arrays have the same normal resistances R and critical currents I_c , that is: there is no statistical variation in the junction parameters. The time-averaged voltage, appearing between the top and bottom bias current leads (Fig. 1), is \bar{v} and is normalised by RI_c . The transfer function \bar{v}_ϕ of a SQUID array is $\bar{v}_\phi = \partial\bar{v}/\partial\phi_a$, where $\phi_a = \Phi_a/\Phi_0$ with Φ_a the applied flux per SQUID cell and Φ_0 the flux quantum. The transfer function \bar{v}_ϕ depends on several parameters, which can be grouped into intrinsic, extrinsic and geometric parameters, where

$$\bar{v}_\phi = \bar{v}_\phi(I_c, T, I_b, \Phi_a, \hat{L}, N_s, N_p). \quad (1)$$

Here, I_c is the only intrinsic parameter as R has been absorbed by normalisation. The three external parameters are the applied temperature T , the applied total bias current I_b and the flux Φ_a applied per SQUID cell. The geometrical parameters are the inductance matrix \hat{L} of the commensurate array, the number N_s of JJ rows in series and the number N_p of JJs in parallel in each row. We fix T at 77 K which is common for YBCO devices.

To obtain optimal flux-to-voltage transduction, the transfer function of the SQUID array can be maximised by adjusting the external bias current I_b and the external applied flux Φ_a such that the transfer function is at its maximum. We denote the maximum transfer function at $i_b = i_b^*$ and $\phi_a = \phi_a^*$ by \bar{v}_ϕ^{\max} .

The theoretical model used here to calculate the maximum transfer functions \bar{v}_ϕ^{\max} and the spectral noise densities is similar to the RSJ simulation model used by Cybart *et al.* [8]. The mathematical model used here has been discussed in detail in a separate publication [22], which takes into account the effect of thermal noise and mutual inductances.

In the following simulations, we keep I_c and \hat{L} fixed while varying the array geometric parameters N_s and N_p . We use $I_c = 20 \mu\text{A}$, which is a typical value for YBCO step edge JJs [12]. The inductance matrix \hat{L} is defined by the commensurate array layout shown in Fig. 1. Here, the square loop width is $a = 10 \mu\text{m}$ with track width $w = 2 \mu\text{m}$ and film thickness $0.2 \mu\text{m}$. The inductance matrix includes the kinetic inductances where the London penetration depth is taken as $\lambda = 0.4 \mu\text{m}$. For the geometric part of the inductance matrix, we use the analytic expressions given in [23].

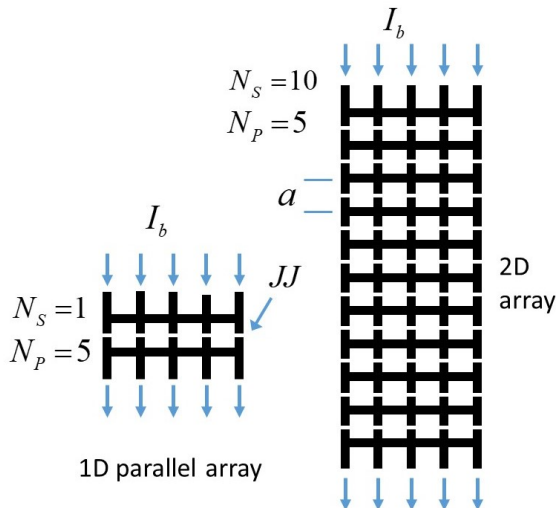


Figure 1: Examples of commensurate thin-film SQUID arrays. On the left, the layout of an $N_p = 5, N_s = 1$, 1D SQUID array and on the right a 2D SQUID array with $N_p = 5, N_s = 10$. The SQUID loop areas are squares with side length a , which is the cell size. The location of the JJs is indicated as gaps. The total biasing current I_b is injected uniformly from the top with each of the N_p leads receiving the same constant current I_b/N_p . A spatially homogeneous magnetic flux ϕ_a per SQUID cell is applied to the array.

From the self-inductance L_s of the individual SQUID loops, one finds $\beta_L = 2I_c L_s / \Phi_0 = 0.76$. The noise strength parameter corresponding to these values and $T = 77$ K is $\Gamma = 2\pi k_B T / (\Phi_0 I_c) = 0.16$, where k_B is the Boltzmann constant. The top and bottom bias leads were taken as $100 \mu\text{m}$ long and their inductances were included in our calculations, though their contributions were found to be negligibly small.

As an example, Fig. 2 shows for $N_p = 5$ the time-averaged voltage \bar{v}/N_s , for $N_s = 1$ (red) and $N_s = 10$ (dashed blue), versus the applied flux ϕ_a for different bias currents $i_b = I_b / (N_p I_c)$ where I_b is the total bias current (see Fig. 1). We see that \bar{v}/N_s depends on i_b . In the case of $N_s = 1$, the maximum transfer function \bar{v}_ϕ^{\max} occurs at $i_b^* = 0.75$ and $\phi_a^* = 0.095$.

By varying N_s and N_p , we find that \bar{v}_ϕ^{\max} occurs at $i_b^* \approx 0.75$, independent of N_s and N_p . In contrast, the applied flux ϕ_a^* varies strongly with N_p . As shown in Fig. 3, ϕ_a^* initially rapidly decreases with increasing N_p . While $\phi_a^* = 0.25$ for the common dc SQUID ($N_s = 1, N_p = 2$), $\phi_a^* \approx 0.075$ if $N_p \gtrsim 6$ for both $N_s = 1$ (1D parallel arrays) as well as $N_s = 10$ and 20 (2D arrays).

Figure 4 shows \bar{v}_ϕ^{\max}/N_s versus N_p for $N_s = 1$ (1D parallel arrays) and $N_s = 10$ and 20 (2D arrays). The maximum transfer function \bar{v}_ϕ^{\max} initially increases

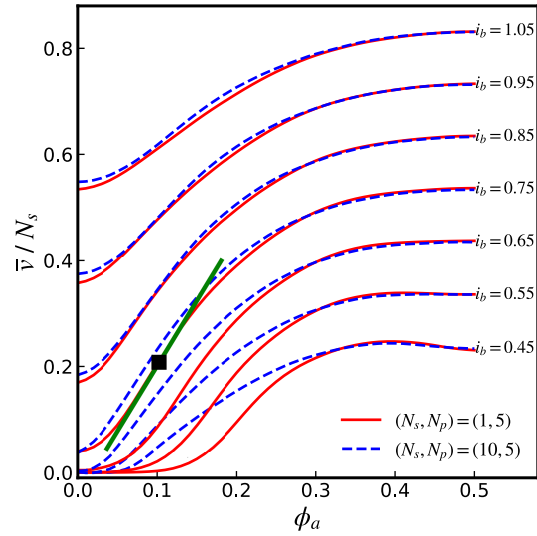


Figure 2: Normalised voltage-flux response of a SQUID array with $N_p = 5$, for different normalised bias currents i_b where $N_s = 1$ (1D parallel array, red) and $N_s = 10$ (2D array, dashed blue). Similar to the common dc SQUID, \bar{v} is symmetric about the origin and translation invariant with period 1. In green we show the maximum slope, defining \bar{v}_ϕ^{\max} for (1,5). The black square denotes ϕ_a^* where \bar{v}_ϕ has its maximum.

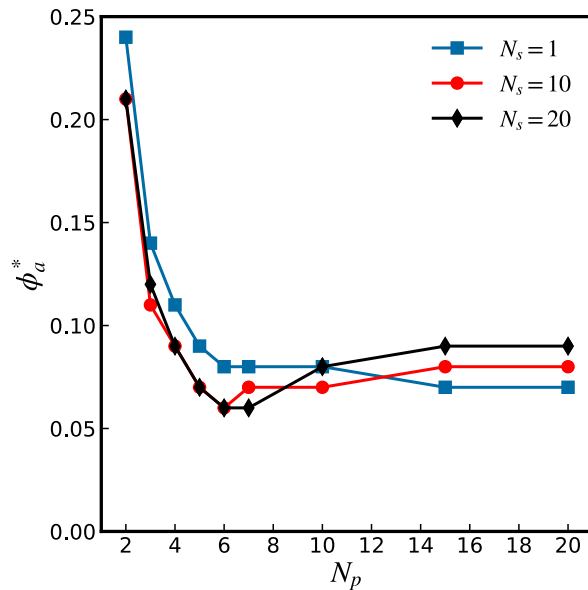


Figure 3: Normalised applied flux ϕ_a^* per SQUID loop which maximises the transfer function \bar{v}_ϕ versus the number N_p of JJs in parallel, for $N_s = 1$ (1D parallel arrays) and $N_s = 10$ and 20 (2D arrays).

with N_p . However, for $N_p \gtrsim 6$, \bar{v}_ϕ^{\max} plateaus for the

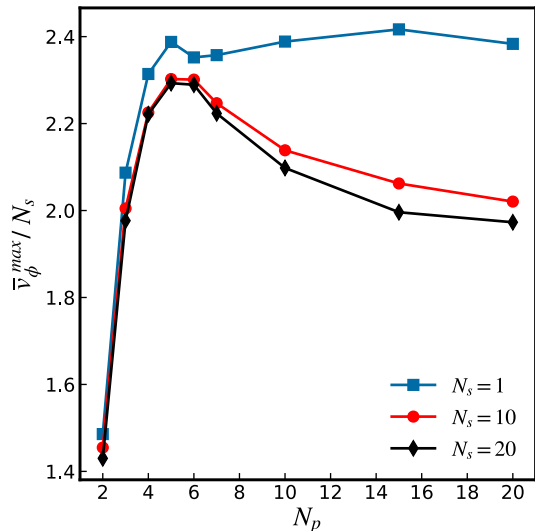


Figure 4: Maximum transfer function \bar{v}_ϕ^{\max}/N_s versus N_p for $N_s = 1$ (1D parallel arrays) and $N_s = 10$ and 20 (2D arrays).

1D parallel arrays and slightly decreases for the 2D arrays. The levelling of \bar{v}_ϕ^{\max}/N_s for $N_p \gtrsim 6$ in Fig. 4 can be understood from calculations performed by Kornev *et al.* [24, 25] and others [26].

3. Array low-frequency voltage and flux noise spectral density

The voltage noise spectral density can be obtained from the Fourier transform of $v(\tau)$. The one-sided voltage noise spectral density $S_v(f)$ in dimensionless units (normalised by $RI_c\Phi_0/(2\pi)$) is given by

$$S_v(f) = \lim_{\tau_0 \rightarrow \infty} \frac{2}{\tau_0} \left| \int_{-\tau_0/2}^{\tau_0/2} v(\tau) e^{i2\pi f\tau} d\tau \right|^2, \quad (2)$$

where i is the unit imaginary number. Here, $v(\tau)$ is the time-dependent total voltage between the bias leads of the array, f is the spectral frequency in dimensionless units, normalised by $2\pi RI_c/\Phi_0$, and τ the time in dimensionless units, normalised by $\Phi_0/(2\pi RI_c)$.

The low-frequency voltage-noise spectral density $S_v(0)$ can be calculated from a low frequency analysis as detailed in Tesche & Clarke [19]. This can be done by averaging the total array voltage $v(\tau)$ of the array, i.e.

$$v(\tau) = \sum_{j=1}^{N_s} \frac{1}{N_p} \sum_{k=1}^{N_p} v_{jk}(\tau), \quad (3)$$

over time intervals $\Delta\tilde{\tau} = 400\Delta\tau$ and obtaining a set of $N = 512$ averaged voltages [27], where $v_{jk}(\tau)$ is

the voltage corresponding to the k th junction (from left to right) in the j th row of the array. We then take the Fourier transform of this discrete set and by using Eq. 2 the low-frequency voltage-noise $S_v(0)$ is determined. To enhance the numerical accuracy, we repeat this process up to 7000 times in order to achieve a good ensemble average for $S_v(0)$. This discrete Fourier transform procedure is accurate subject to the condition $f_J \ll 1/\Delta\tilde{\tau} \ll Nf_J$ [19], where f_J is the normalised fundamental Josephson frequency $\bar{v}(i_b^*, \phi_a^*)/2\pi$. In our simulations, we use $\Delta\tau = 0.01$. In this paper, we limit the size of our arrays to no more than $(20, 20)$ due to the large computation times required to accurately compute S_v .

As the Johnson noise voltages of the JJ's are uncorrelated and their mean square deviations are identical, one would simplistically expect to obtain the scaling behaviour

$$S_v(0) \propto \frac{N_s}{N_p}. \quad (4)$$

This is evident from Eq. 2 and 3: $v(\tau)$ is calculated by taking the arithmetic mean of the junction voltages in parallel, and then summing up the voltage in series for N_s rows.

Similar to $S_v(0)$, the voltage to voltage-noise ratio SNR_v is expected to follow the scaling behaviour

$$SNR_v \propto \frac{N_s}{(N_s/N_p)^{1/2}} = (N_s N_p)^{1/2}. \quad (5)$$

Using our above mentioned 2D SQUID array model, we have calculated the normalised low-frequency voltage-noise spectral density $S_v(0)$ from Eq.2 for 1D parallel arrays and 2D arrays.

Figure 5 shows $S_v(0)$ versus N_p for $N_s = 1$ (1D parallel arrays) and $N_s = 10$ and 20 (2D arrays) calculated at ϕ_a^* (Fig. 3) and i_b^* where the transfer functions \bar{v}_ϕ have their maxima. The dashed curves indicate the N_s/N_p scaling behaviour. The calculation shows that the voltage noise spectral density $S_v(0)$ for the 1D parallel arrays does not follow the N_s/N_p scaling but instead, $\sim N_s/N_p^{0.3}$. In contrast, the 2D arrays follow the N_s/N_p scaling fairly well.

It is also useful to plot $S_v(0)$ relative to the normalised Johnson white noise voltage spectral density $S_v^R(0)$ for a purely resistive array with resistance $N_s R/N_p$. Since the de-normalised white-noise voltage spectral density of a resistor R is $4k_B T R$ [28], one finds $S_v^R(0) = 4\Gamma N_s/N_p$ where Γ is the noise strength. Using the data from Fig. 5, Fig. 6 shows $S_v(0)/(4\Gamma N_s/N_p) = S_v(0)/S_v^R(0)$ versus N_p for different N_s . Figure 6 clearly reveals the deviations from the N_s/N_p scaling, where for perfect scaling the data would follow horizontal lines like the dashed green line. In particular, the 1D parallel arrays ($N_s = 1$, in red) do not follow the scaling. The orange dashed

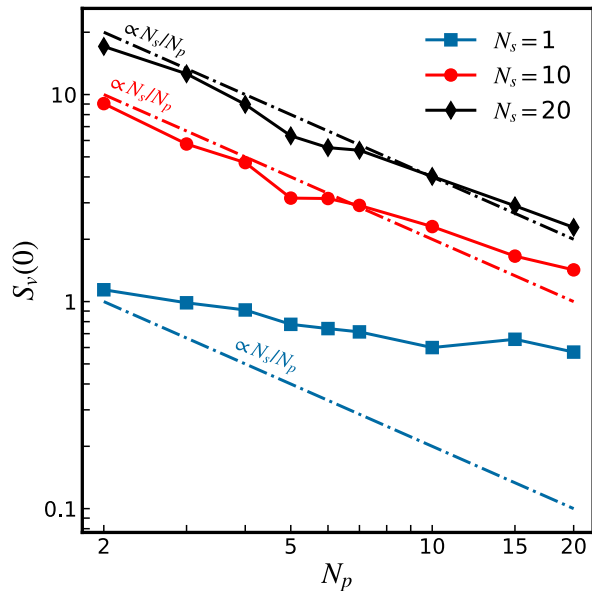


Figure 5: Low-frequency voltage-noise spectral density $S_v(0)$ versus N_p for $N_s = 1$ (1D parallel arrays) and $N_s = 10$ and 20 (2D arrays). The dashed green curves show the scaling N_s/N_p of Eq. 4.

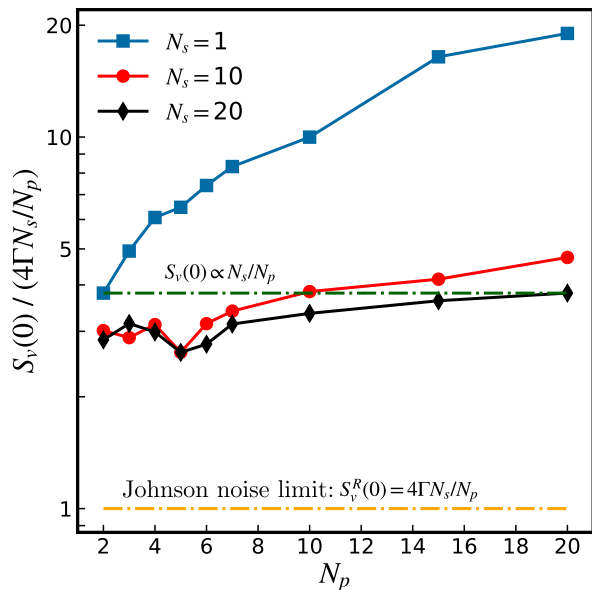


Figure 6: Low-frequency normalised voltage noise spectral density $S_v(0)/(4\Gamma N_s/N_p)$ versus N_p for $N_s = 1$ (1D parallel arrays) and $N_s = 10$ and 20 (2D arrays). The dashed green curve shows the scaling N_s/N_p of Eq. (5). In orange the Johnson noise limit.

horizontal line in Fig. 6 is the Johnson noise limit, i.e. $S_v^R(0) = 4\Gamma N_s/N_p$, and the 2D SQUID arrays with relatively large N_s get closest to this limit.

Kornev *et al.* [29, 24] have shown that such a

behaviour for $S_v(0)$ in 1D parallel arrays occur due to the emergence of a finite JJ interaction radius [25] but they did not examine the behaviour of 2D arrays.

In practice, the rms flux noise $S_\phi^{1/2}(f)$ is used as a measure of the device's performance. It is given by the expression

$$S_\phi^{1/2}(f) = \frac{S_v^{1/2}(f)}{\bar{v}_\phi}. \quad (6)$$

Since \bar{v}_ϕ approximately scales with N_s , one expects for $S_\phi^{1/2}(0)$ the scaling behaviour

$$S_\phi^{1/2}(0) \propto (N_s N_p)^{-1/2}, \quad (7)$$

and for the flux to flux-noise ratio, SNR_ϕ ,

$$\text{SNR}_\phi \propto (N_s N_p)^{1/2}, \quad (8)$$

which is the same scaling as for SNR_v in Eq. 5.

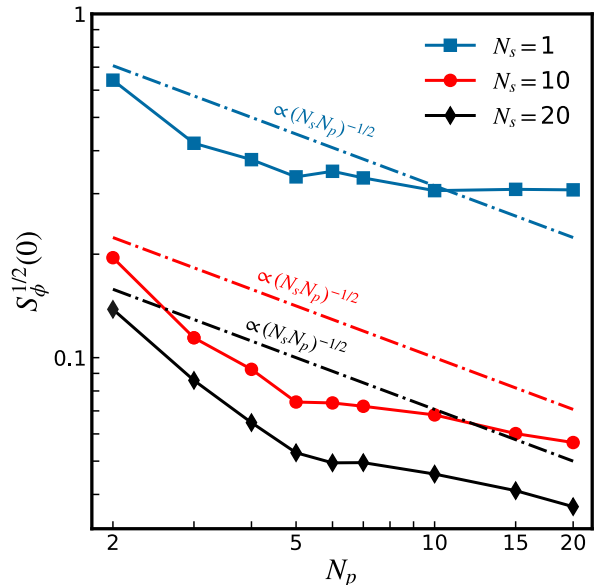


Figure 7: Low-frequency rms flux noise $S_\phi^{1/2}(0)$ versus N_p for $N_s = 1$ (1D parallel arrays) and $N_s = 10$ and 20 (2D arrays). The dashed lines show the scaling $(N_s N_p)^{-1/2}$.

Figure 7 shows the calculated low-frequency rms flux noise $S_\phi^{1/2}(0)$ versus N_p for different N_s . The $S_\phi^{1/2}$ were obtained from Eq. 6 at ϕ_a^* and i_b^* . As can be seen, for the three different N_s the deviations from the $S_\phi^{1/2} \propto (N_s N_p)^{-1/2}$ scaling (dashed straight lines) are similar. This is due to the \bar{v}_ϕ^{-1} factor in Eq. 6.

A revealing measure for the rms flux noise of a SQUID array is the dimensionless quantity $\xi_\Phi^{1/2}$ defined as

$$\xi_\Phi^{1/2} = \frac{S_\phi^{1/2}(0)}{(4\Gamma/N_s N_p)^{1/2}}. \quad (9)$$

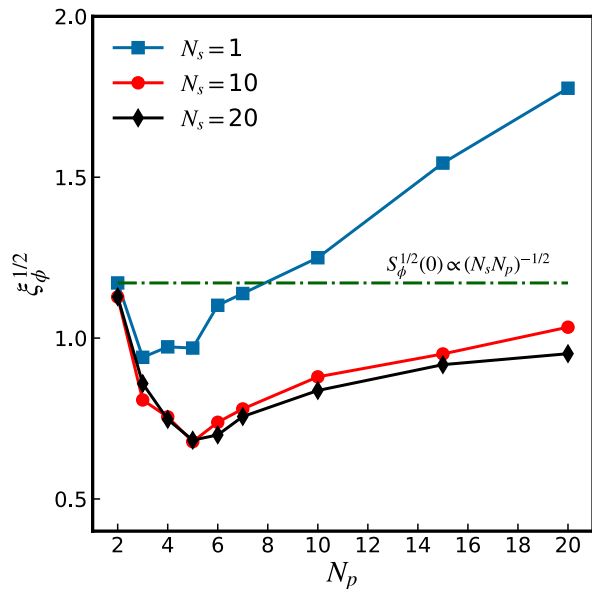


Figure 8: Low-frequency rms flux noise measure $\xi_\phi^{1/2}$ defined by Eq. 9 versus N_p for $N_s = 1$ (1D parallel arrays) and $N_s = 10$ and 20 (2D arrays). The dashed green curve shows the scaling $(N_s N_p)^{-1/2}$ of Eq. 7.

The result for Eq. 9, evaluated at ϕ_a^* and i_b^* , is displayed in Fig. 8 showing $\xi_\phi^{1/2}$ versus N_p for different N_s . Compared to Fig. 7, Fig. 8 reveals the relative deviation from the $\sim (N_s N_p)^{-1/2}$ scaling. In the case of perfect scaling, the data would lie on horizontal straight lines similar to the green dashed line.

It is important to note that the values (i_b^*, ϕ_a^*) which maximise \bar{v}_ϕ do not minimise the voltage noise $S_v(0)$. Figure 9 shows the distribution of \bar{v}_ϕ and $S_v(0)$ values for a range of i_b and ϕ_a , not just i_b^* and ϕ_a^* . Similarly, one can plot $S_\phi^{1/2}(0)$ for multiple (i_b, ϕ_a) and see how it compares to \bar{v}_ϕ . Figure 10 shows several $S_\phi^{1/2}$ heatmaps for differently-sized arrays. They show that $S_\phi^{1/2}(0)$ is approximately minimised in the neighbourhood where \bar{v}_ϕ is a maximum for the (1,2) and (1,20)-arrays. However, this is not the case for the (20,20)-array, which indicates that one cannot optimise both the transfer function and noise of the array with the same (i_b^*, ϕ_a^*) values for arrays of arbitrary size.

We now proceed to de-normalise the normalised voltage noise spectral density S_v . This is done by multiplying S_v by $RI_c\Phi_0/2\pi$. Using $R = 10\Omega$ [1], we compute the rms voltage spectral density $S_V^{1/2}$ for different SQUID cell sizes a and show the results in Fig. 11.

In a similar manner, one can de-normalise the normalised transfer function \bar{v}_ϕ to obtain $\bar{V}_B = \partial\bar{V}/\partial B_a$. This is achieved by multiplying \bar{v}_ϕ by $RI_c A_{\text{eff}}/\Phi_0$ where A_{eff} is the effective area of the

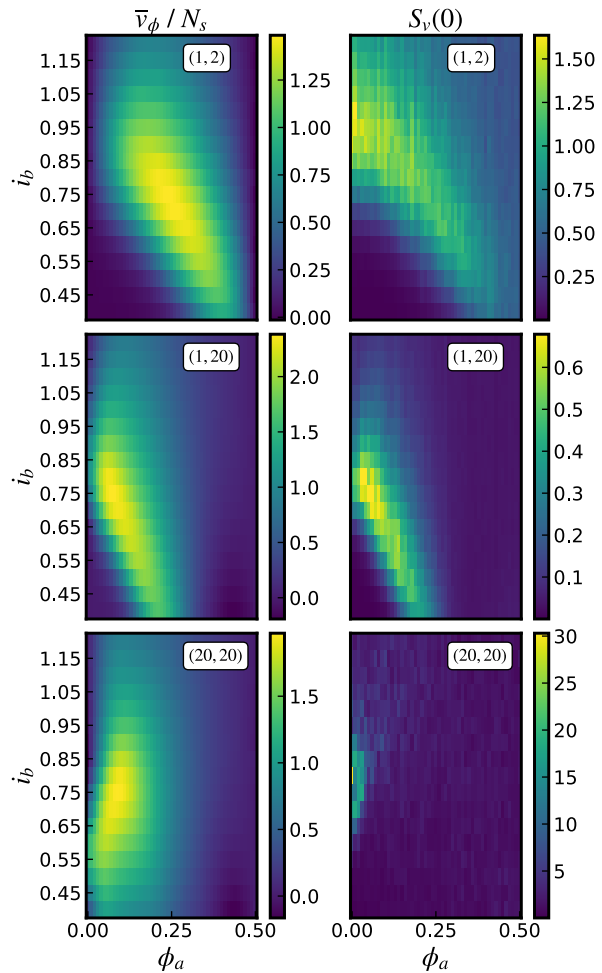


Figure 9: Normalised transfer function and voltage noise spectral density as functions of i_b and ϕ_a for SQUID arrays of varying sizes.

SQUID cell, which in our case is $A_{\text{eff}} = a^2$. The results for \bar{V}_B^{max} as a function of a are shown in Fig. 12.

The normalised rms flux noise $S_\phi^{1/2}$ is de-normalised by multiplying $S_\phi^{1/2}$ with $\gamma = \Phi_0^{3/2}/\sqrt{2\pi RI_c}$. Using again the junction parameters at $T = 77$ K of $R = 10\Omega$ and $I_c = 20\mu\text{A}$ one obtains $\gamma = 1.28\mu\Phi_0/\sqrt{\text{Hz}}$. Using the normalised $S_\phi^{1/2}$ value from Fig. 10 corresponding to the (20,20)-array, one finds an rms flux noise of $0.05\mu\Phi_0/\sqrt{\text{Hz}}$. In contrast, the rms flux noise of the (1,20)-array is 10 times higher, while according to the scaling behaviour in Eq. (8) it should be ≈ 4.5 times higher.

The rms magnetic field noise spectral density $S_B^{1/2}$ is obtained by dividing the rms flux noise by the SQUID loop area a^2 , or simply by calculating $S_V^{1/2}/\bar{V}_B^{\text{max}}$. This gives for the $N_s = N_p = 20$ array with $a^2 = 100\mu\text{m}^2$ a value of $S_B^{1/2} = 1.0\text{pT}/\sqrt{\text{Hz}}$. This result is consistent with the literature, for instance

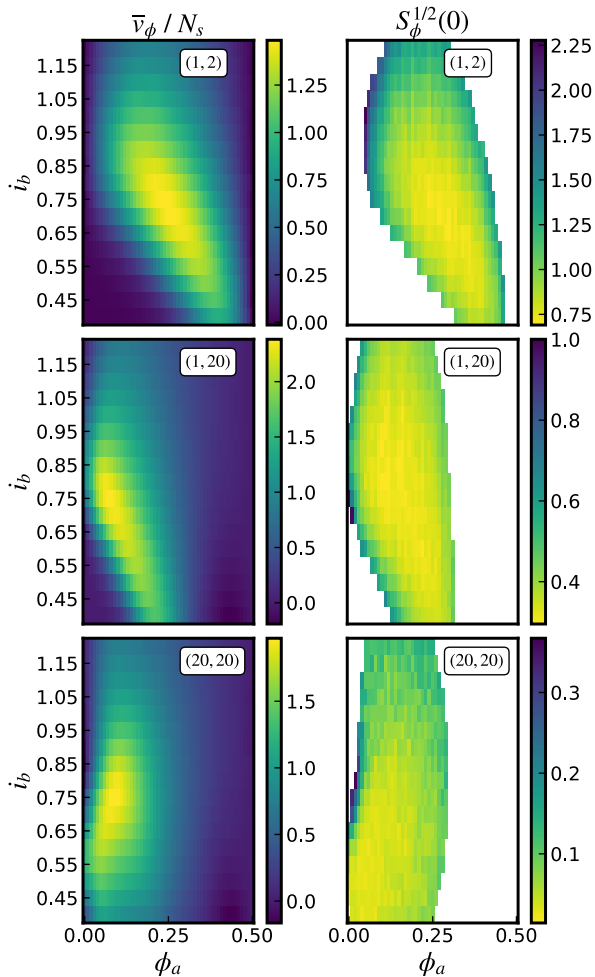


Figure 10: Normalised transfer function and flux noise spectral density as functions of i_b and ϕ_a for SQUID arrays of varying sizes. The blank white regions correspond to points where $\bar{v}_\phi/N_s \rightarrow 0$ and have been excluded from the plots to improve visibility of the smaller $S_\phi^{1/2}(0)$ values.

Couëdo *et al.* [30] reported a white noise measurement of ≈ 300 fT/ $\sqrt{\text{Hz}}$ on a (300,2)-SQIF array made of YBCO and operating at $T = 66$ K. By contrast, in low-temperature dc-SQUIDs operating at $T \leq 4.2$ K, one often finds $S_B^{1/2} \approx 1 - 4$ fT/ $\sqrt{\text{Hz}}$ using pick-up coils (see for instance Drung *et al.* [31, 32]). Similarly, earlier work on high- T_c YBCO dc-SQUIDs operating at 77 K showed that by coupling the SQUID to a large pickup loop of millimetre size, that $S_B^{1/2}$ could be reduced down to ≈ 10 fT/ $\sqrt{\text{Hz}}$ [33].

In the case of SQUID arrays, $S_B^{1/2}$ can be reduced further by increasing \bar{V}_B^{\max} . For instance, Fig. 13 shows $S_B^{1/2}$ as a function of a , and we see that increasing both N_s and N_p contributes to a reduction in noise. Furthermore, since $S_V^{1/2}$ is relatively flat

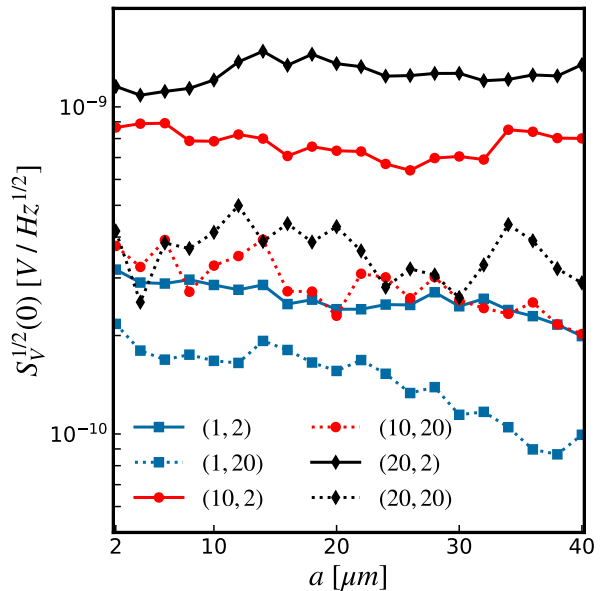


Figure 11: RMS voltage noise spectral density at $T = 77$ K for different cell sizes a and array configurations. The range of a corresponds to a β_L range from 0.1 to 3.8.

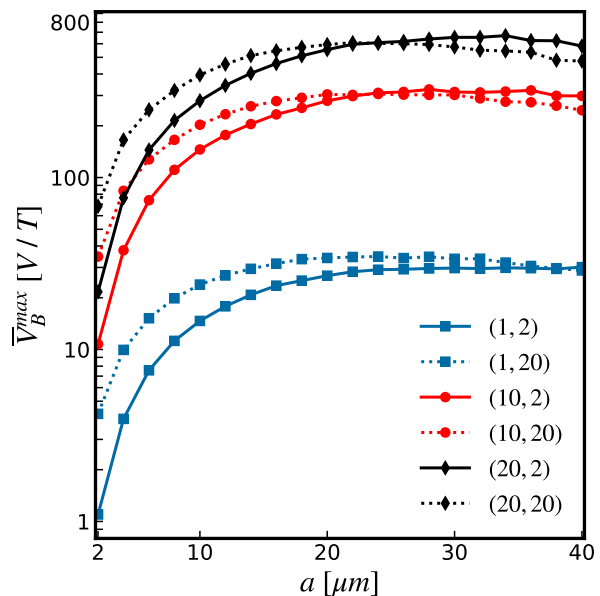


Figure 12: Maximum transfer function at $T = 77$ K for a range of cell sizes a and array configurations. The range of a corresponds to a β_L range from 0.1 to 3.8.

with a as shown in Fig. 11, and \bar{V}_B^{\max} increases with a but plateaus beyond $a = 20 \mu\text{m}$, $S_B^{1/2}$ in Fig. 13 stops decreasing for larger a . The lowest noise level achieved in Fig. 13 is ~ 450 fT/ $\sqrt{\text{Hz}}$ for a (20,20)-array with loop-size $a = 30 \mu\text{m}$, which represents a two-fold improvement from the array with loop-size $a = 10 \mu\text{m}$.

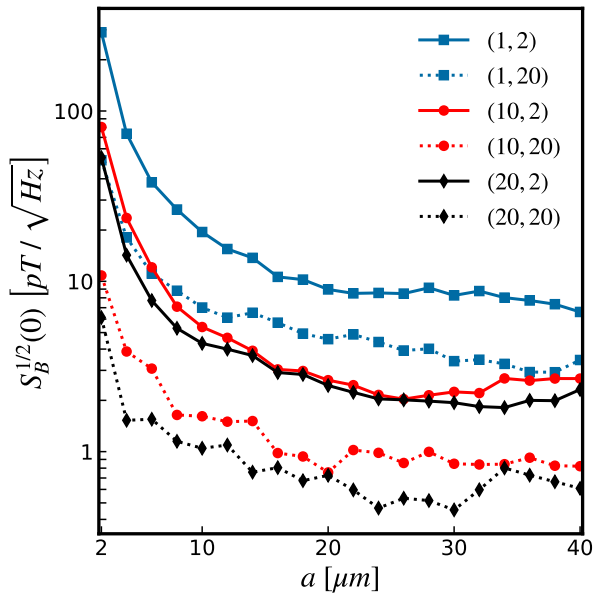


Figure 13: Magnetic field noise spectral density at $T = 77$ K for a range of cell sizes a and array configurations. The range of a corresponds to a β_L range from 0.1 to 3.8.

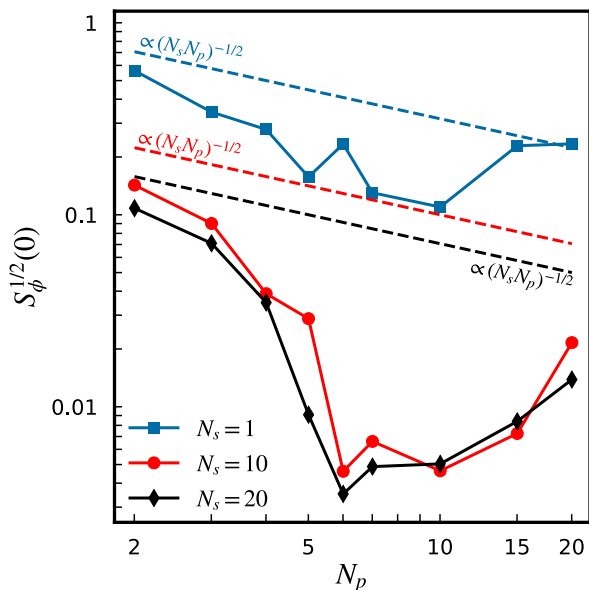


Figure 14: Normalized rms flux noise $T = 77$ K as a function of N_s and N_p when using the values (i_b, ϕ_a) which minimize $S_\phi^{1/2}(0)$ instead of maximizing \bar{v}_ϕ .

It should be noted that variations in the parameters can change the simulation results. From Figures 12 and 13, one sees an increase in the maximum transfer function \bar{V}_B^{\max} with increasing β_L for constant I_c , which in turn leads to a decrease in the magnetic field density noise $S_B^{1/2}(0)$. If one instead keeps the loop

area constant, but varies the I_c of the JJs; one obtains different results from the ones presented in this paper. For instance, choosing a lower I_c decreases \bar{V}_B^{\max} but increases the magnetic field density noise $S_B^{1/2}(0)$, while a higher I_c increases \bar{V}_B^{\max} but lowers $S_B^{1/2}(0)$. This is consistent with the fact that since $\beta_L \sim I_c$ and $\Gamma \sim 1/I_c$, one expects the noise level to decrease as I_c grows larger. This implies one can further improve the device's robustness to noise by increasing the critical current of the junctions.

Lastly, we must discuss the case in which (i_b, ϕ_a) are selected to minimize $S_\phi^{1/2}(0)$ instead of maximizing \bar{v}_ϕ . Fig. 14 shows the minimized $S_\phi^{1/2}(0)$ as a function of N_p and N_s , which exhibits a significantly different trend to Fig. 7: the rms flux noise has a clear minimum near $N_p \approx 6$ which becomes more prominent for larger N_s . At $N_s = 20$ and $N_p = 6$, $S_\phi^{1/2}(0) = 0.0035$ which is over 10 times smaller than in Fig. 7. However, this comes at the cost of a smaller transfer function: in this case, $\bar{v}_\phi/N_s \approx 0.367$ compared to the optimum $\bar{v}_\phi/N_s \approx 2.28$ in Fig. 4. This shows that the choice of (i_b, ϕ_a) can either maximise \bar{v}_ϕ or minimise $S_\phi^{1/2}(0)$, but not both simultaneously.

4. Conclusion

In this paper, we have shown through numerical simulations how the noise scales in 1D and 2D SQUID arrays with respect to the number of junctions. In 1D SQUID arrays we observed a $\sim N_s/N_p^{0.3}$ voltage noise spectral density scaling. In contrast, the voltage noise spectral density of 2D arrays follows the $\sim N_s/N_p$ scaling closely. Though increasing N_p beyond a certain value will not further increase the maximum transfer function, it further reduces the voltage noise spectral density. The rms flux noise, which is inversely proportional to the transfer function; deviates from the expected $\sim (N_s N_p)^{-1/2}$ scaling for both the 1D parallel arrays and the 2D arrays when \bar{v}_ϕ is optimised. Furthermore, we have shown that one cannot optimise the transfer function as well as the flux noise of the array using the same bias current and flux values unless $N_s = 1$. By varying the cell size for a given array (N_s, N_p) , one can further reduce the magnetic field noise spectral density without compromising the maximum transfer function. This indicates that there is still room for exploration in the improvement of high- T_c SQUID arrays for sensing applications.

References

- [1] Clarke, J. and Brakinski, A. 2006 *Wiley-VCH, Weinheim*.
- [2] Fagaly, R. L. 2006 *Rev. Sci. Instruments* **77** 101101.
- [3] Miller, J. H. and Gunaratne, G. H. and Huang, J. and Golding, T. D. 1991 *Appl. Phys. Lett.* **59** 3330.

- [4] Oppenländer, J. and Häussler, Ch and Schopohl, N. 2000 *Phys. Rev. B* **63** 024511.
- [5] Müller, K–H. and Mitchell, E. E. 2021 *Phys. Rev. B* **103** 054509.
- [6] Müller, K–H. and Mitchell, E. E. 2024 *Phys. Rev. B* **109** 054507.
- [7] Longhini, P. and Berggren, S. and Palacios, A. and In, V. and de Escobar, A. L. 2011 *IEEE TRans. Appl. Supercond.* **21** 391.
- [8] Cybart, S. A. and Dalichaouch, T. N. and Wu, S. M. and Anton, S. M. and Drisko, J. A. and Parker, J. M. and Harteneck, B. D. and Dynes, R. C. 2012 *J. Appl. Phys.* **112** 063911.
- [9] Dalichaouch, T. N. and Cybart, S. A. and Dynes, R. C. 2014 *Supercond. Sci. Technol.* **27** 065006.
- [10] Taylor, B. J. and Berggren, S. A. E. and O’Brian, M. C. and deAndrade, M. C. and Higa, B. A. and Leese de Escobar, A. M. 2016 *Supercond. Sci. Technol.* **29** 084003.
- [11] Cho, E. Y. and Zhou, Y. W. and Khapaev, M. M. and Cybart, S. A. 2019 *IEEE Trans. Appl. Supercond.* **29** 1601304.
- [12] Mitchell, E. E. and Müller, K–H. and Purches, W. E. and Keenan, S. T. and Lewis, C. J. and Foley, C. P. 2019 *Supercond. Sci. Technol.* **32** 124002.
- [13] Ramos, J. and Zakosarenko, V. and Ijsselsteijn, R. and Stolz, R. and Schultze, V. and Chwala, A. and Hoenig, H. E. and Meyer, H. G. 1999 *Supercond. Sci. Technol.* **12** 597.
- [14] Bruno, A. C. and Espy, M. A. 2004 *Supercond. Sci. Technol.* **17** 908.
- [15] Kornev, V. K. and Soloviev, I. I. and Klenov, N. V. and Mukhanov, O. A. 2010 *IEEE Trans. Appl. Supercond.* **21** 394–398.
- [16] Zhou, X. and Schmitt, V. and Bertet, P. and Vion, D. and Wustmann, W. and Shumeiko, V. and Esteve, D. 2014 *Phys. Rev. B* **89** 214517.
- [17] Chesca, B. and John, D. and Mellor, C. J. 2015 *Appl. Phys. Lett.* **107** 16.
- [18] Chesca, B. and John, D. and Cantor, R. 2021 *Appl. Phys. Lett.* **118** 4.
- [19] Tesche, C. D. and Clarke, J. 1977 *J. Low Temp. Phys.* **29** 301.
- [20] Bruines., J. J. P. and de Waal, V. J. and Mooij, J. E. 1982 *J. Low Temp. Phys.* **46** 383.
- [21] Kleiner, R. and Koelle, D. and Ludwig, F. and Clarke, J. 2004 *Proceedings of the IEEE* **92** 10 1534–1548.
- [22] Galí Labarias, M. A. and Müller, K–H. and Mitchell, E. E. 2022 *Phys. Rev. Appl.* **17** 064009.
- [23] Hoer, C. and Love, C. 1965 *J. Res. Nat. Bureau Standards C. Eng. Instrum.* **69** 127.
- [24] Kornev, V. K. and Soloviev, I. I. and Klenov, N. V. and Filippov, T. V. and Engseth, H. and Mukhanov, O. A. 2009 *IEEE Trans. Appl. Supercond.* **19** 916.
- [25] Kornev, V. K. and Soloviev, I. I. and Klenov, N. V. and Mukhanov, O. A. 2011 *IEEE Trans. Appl. Supercond.* **21** 394.
- [26] Galí Labarias, M. A. and Müller, K–H. and Mitchell, E. E. 2022 *IEEE Trans. Appl. Supercond.* **32** 1600205.
- [27] Enpuku, K. and Muta, T. and Yoshida, K. and Irie, F. 1985 *J. Appl. Phys.* **5** 1916.
- [28] Nysquist, H. 1928 *Phys. Rev.* **32** 110.
- [29] Kornev, V. K. and Arzumanov, A. V. 1997 *Inst. Phys. Conf. Ser., IOP Publishing Ltd.* **158** 627.
- [30] Couëdo, F. and Recoba Pawlowski, E. and Kermorvant, J. and Trastoy, J. and Crété, D. and Lemaitre, Y. and Marcilhac, B. and Ulysse, C. and Feuillet-Palma, C. and Bergeal, N. 2019 *Appl. Phys. Lett.* **114** 19.
- [31] Drung, D. 1991 *Supercond. Sci. Technol.* **4** 377.
- [32] Drung, D., Abmann, C., Beyer, J., Kirste, A., Peters, M., Ruede, F. and Schurig, T. 2007 *IEEE Trans. Appl. Supercond.* **17** 699–704.
- [33] Koelle, D. and Kleiner, R. and Ludwig, F. and Dantsker, E. and Clarke, J. 1999 *Rev. Mod. Phys.* **71** 631.